The impact of hydrogen enrichment on the flow field evolution in turbulent explosions

Tao Li, Fabian Hampp, R. Peter Lindstedt*

Department of Mechanical Engineering, Imperial College, Exhibition Road, London SW7 2AZ, United Kingdom

ARTICLE INFO

ABSTRACT

The reactivity of fuel-air mixtures has a strong impact on the severity of obstacle-induced turbulent explosions. While the influence on the flame speed and pressure development has been studied for a wide range of mixtures at different physical scales, the experimental quantification of the resulting flow fields, e.g. in the critical recirculation zones behind obstacles, is typically absent. The lack of such data presents a serious impediment to the development of reliable predictive methods. The current study reports velocity measurements obtained from highly reproducible experiments performed in a flame tube with two staggered obstacles using fuel lean $H_2/CH_4/Air$ and $H_2/CO/Air$ mixtures at a stoichiometry of 0.60. The mixture reactivity for both fuels was varied using H_2 substitution levels of 50% and 80% with the pure hydrogen (100%) case used as a reference. The flow field was quantified using high-speed (10 kHz) particle image velocimetry (PIV), time-series PIV and Mie scattering. The time-resolved evolution of the recirculation zone behind the second obstacle was successfully captured with the explosion over-pressure and flame propagation speed also measured. Data is presented for the mean horizontal ($\bar{u}$) and vertical ($\bar{v}$) velocity components at 18 spatial locations for each mixture along with the translational velocities of the shear driven recirculating eddies formed behind the second obstacle. It is shown that the temporal evolution of the flows (not velocity magnitudes) can be approximately normalised based on the flame arrival at the second obstacle. The data provides a comprehensive quantitative description of the flow field evolution leading up to explosion events and is expected to facilitate model development.

1. Introduction

The use of hydrogen enriched fuel blends is of increasing practical relevance due to improvements in flame stability under fuel lean conditions with corresponding benefits for reduced carbon dioxide emissions [1–3]. The resulting mixture reactivity also has a direct impact on flame propagation speeds and explosion over-pressures and also impacts turbulence–chemistry interactions. For example, Lee et al. [4] showed that flame acceleration in a round obstructed tube using hydrogen/air mixtures with H_2 contents from 10% to 45% resulted in different propagation modes such as quenching, quasi-detonations and Chapman–Jouget (CJ) detonations. Cammarota et al. [5] and Salzano et al. [6] studied the explosion behaviour of $H_2/CH_4/Air$ mixtures and found that a low hydrogen content (up to 10% by volume) has a negligible impact on the over-pressure, while the effect becomes dramatic for amounts exceeding 50%. Lowesmith et al. [7] reported a small increase in flame speed and over-pressure with H_2 substitution for CH_4 up to

20% and a significant increase for 50% in a series of large scale explosion experiments. Schiavetti and Carcassi [8] experimentally studied the influence of the H_2 concentration on the maximum over-pressure in vented deflagrations. A non-monotonic behaviour of the developed peak pressure as a function of hydrogen concentration was observed at 11% of H_2 by volume and the reason was attributed to the interactions of the flame front with acoustic waves. Li et al. [9] measured flame speeds and over-pressures generated in an obstructed flame tube with two obstacles installed in a staggered arrangement for a wide range of hydrogen enriched CO and CH_4 mixtures. A distinctly different impact of H_2 substitutions on the explosion behaviours for the two mixture types was reported with CH_4 showing a stronger tendency to reduce the reactivity. A new scaling factor (β), based on the amount of air required to fully oxidise all fuel components, was found to reasonably correlate the impact of fuel composition on the explosion over-pressures. Large scale experiments under vented conditions were conducted by Bauwens et al. [10,11], showing that the peak pressure was a result of the mixture reactivity, flame area and the external explosion caused by the ejection of reactants.
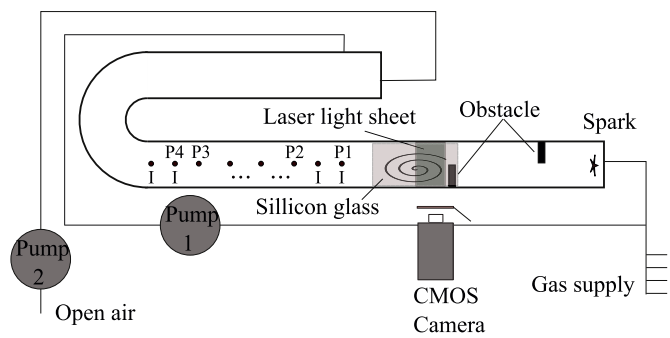
Fig. 1. Schematic of the experimental test facility (P – Pressure transducer, I – Ionisation probe detector).

It is widely accepted that turbulence can increase the explosion over-pressure via enhanced burning velocities [12–14]. Obstacles in the flame path enhance the flame speed significantly by increasing the flame surface area with the resulting positive feedback mechanism well established. Past studies have covered a broad range of parameters such as the blockage ratio, obstruction type and obstacle separation distances under conditions that may lead to a deflagration to detonation transition (DDT) through continuous flame acceleration [15–23]. Ciccarelli and Dorofeev [24] suggest that the burning velocity can be increased 10 – 20 times the laminar burning velocity before local quenching becomes a limiting factor. Bradley et al. [20] evaluated the possibility of DDT and presented a numerical model for the calculation of the maximum turbulent burning velocity a flammable mixture can attain.

The quantitative influence of the mixture reactivity on the flow field evolution has, by contrast, not been extensively investigated due to experimental challenges. Johansen and Ciccarelli [25] visualised the flow field structure ahead of flames in an obstructed channel using a novel Schlieren based photographic technique where helium gas was injected ahead of the flame as a tracer. Lindstedt and Sakthitharan [26] used laser doppler anemometry (LDA) to quantify the flow field in the recirculation region behind an obstacle at high Reynolds numbers ($Re > $ 100,000 and 2000 $< Re_t <$ 4000) in a flame tube. Hampp and Lindstedt [27] performed 10 kHz PIV measurements in the recirculation region behind a single obstacle with a turbulence-generating cross fractal grid (CFG) installed between the obstacle and ignition spark. The influence of initial turbulence was investigated by Bauwens and Dorofeev [28] in a vented chamber with the turbulence generated via four symmetrically installed mixing fans. The flame speed and over-pressure increased with initial turbulence. It was concluded

that the turbulence primarily increased the initial flame wrinkling with the growth rate less affected. Hisken et al. [29] mitigated the explosion over-pressure by up to 33% through passively suppressing the vortex shedding behind bluff-bodies via splitter plates and helical steel wires. The vortex shedding process was visualised via high-speed imaging (4000 fps). Cross and Ciccarelli [30] measured the detonation wave propagation in an obstacle filled tube using ionisation probe detectors, highlighting the critical role of shock reflection in the propagation of quasi-detonation waves. Boeck et al. [31,32] investigated turbulence-flame effects, shock-flame interactions and the flame propagation in an obstructed tube using high-speed hydroxyl planar laser induced fluorescence (OH-PLIF). However, a systematic study of the influence of mixture reactivity on the temporal evolution of velocity fields leading up to turbulent explosions has yet to be reported.

The current study presents results from highly reproducible experiments performed in an obstructed flame tube using five syngas related H_2/CH_4 and H_2/CO mixtures related to fuel lean operation in practical devices. The mixture reactivity was varied using H_2 substitutions of 50% and 80% with the 100% hydrogen case used as a reference point. The flame propagation was quantified using high-speed (10 kHz) particle image velocimetry (PIV), time-series PIV and Mie scattering. Data is presented for the temporal evolution of the mean horizontal ($\bar{u}$) and vertical ($\bar{v}$) velocity components at 18 spatial locations for each mixture. The translational velocities of the shear driven recirculating eddies, flame speeds and over-pressures are also presented. It is expected that the data sets will support the development of improved models for turbulent explosions.

2. Experimental setup

A spark ignited flame tube, schematically depicted in Fig. 1, with physical dimensions provided in Fig. 2, was used in the current study. The configuration consisted of optical and driven sections with a rectangular cross-section of 34 (width) × 72 mm (height) and a cylindrical end section with an internal diameter of 80 mm. The length to hydraulic diameter ratio (L/d) of 155 removed acoustic wave reflections from the non-ignition end for a sufficient time window to provide highly reproducible measurements within the optical section. Two solid obstacles with a thickness of 5 mm and a height of 36 mm (blockage ratio of 50%), were installed at distances of 80 and 400 mm from the ignition end in a staggered arrangement to promote flame acceleration.

A standard electronic ignition device (Sparkrite SX1000; EDA Sparkrite, Ltd.) delivering of the order of 5 mJ [33] via a single spark was installed at the upstream end of the flame tube as
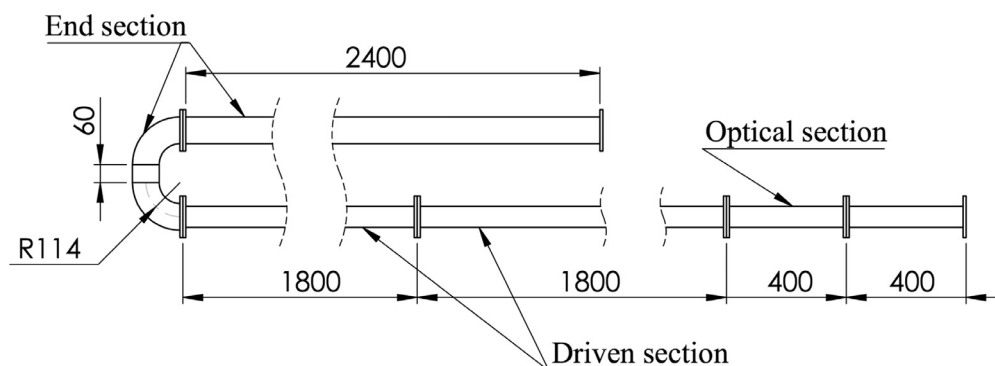

Fig. 2. Dimensions of the flame tube (unit: mm).

Table 1

Locations (X) of pressure transducers (P) and ionisation probe (I) detectors from the ignition point.

X [m]	0.845	1.075	1.305	1.535	2.000	2.225	3.145	3.450
Sensor	P1+I	I	P2+I	I	I	P3+I	P4+I	I

Table 2

Physical properties of the gas mixtures at a constant stoichiometry ($\Phi = 0.60 \pm 0.02$) and the corresponding timing between double laser pulses (Δt), where ρ_0, μ ($\times 10^{-5}$), τ and S_L are the density of the unburned gas mixture, dynamic viscosity, expansion ratio and laminar burning velocity, respectively. The scaling factor β is defined by Eq. (1).

Mixture	H_2 [%]	β	ρ_0 [kg/m³]	μ [Pa · s]	τ	S_L [m/s]	Δt [μs]
H_2/Air	100	1	0.47	1.84	4.52	0.85	6
H_2/CH_4/Air	50	0.20	0.55	1.82	4.58	0.25	15
	80	0.50	0.52	1.83	4.55	0.48	15
H_2/CO/Air	50	0.50	0.53	1.84	4.71	0.52	15
	80	0.80	0.49	1.84	4.60	0.71	10

indicated in Fig. 1. The effect of the ignition energy was found negligible for (stored) values below 100 mJ in a related configuration [34]. Eight ionisation probes were mounted along the tube and served as flame arrival detectors. The ionisation probes were made from a coaxial stainless steel cable with an outer diameter of 1.5 mm and a resistance > 10 MΩ between the core and the shield [35]. The data acquisition card processing the ionisation probe signals featured a response time of 1 μs. The pressure was measured using four piezo-electric pressure transducers (1 × PCB 113A21 and 3 × PCB 113B21; PCB Piezotronics, Inc.) and recorded using a 12-bit data acquisition card (PCI-6115; National Instruments) with a recording rate of 1 MHz. The positions of the pressure transducers and ionisation probe detectors are specified in Table 1.

2.1. Experimental procedure

The flame tube was flushed with air before each experiment for one minute to remove any remaining exhaust gases. Subsequently, the tube was evacuated to a pressure below 5 kPa via a rotary vane pump (RE 2.5; VACCUBRAND GmbH). Leak tests were performed on a regular basis to ensure identical conditions. The leak rate was < 16 Pa/s compared to a filling time of around 45 s. The explosive atmosphere was created using mixtures of dry filtered air, CH_4 (purity 99.5%), CO (99.97%) and H_2 (99.99%) via a partial pressure method with the pressure monitored using a static pressure transducer (UNIK 5000; GE Measurement & Control). The injection of reactants was controlled via digital mass flow controllers (Bronkhorst UK LTD) with uncertainties ≤ 0.8% of the reading plus ≤ 0.2% of full scale [36]. Subsequently, the gas mixture was

circulated for ten minutes, corresponding to 23 tube-volumes, in order to ensure homogeneity. All experiments were repeated a minimum of three times (the 80% H_2 cases four times) for each data point and conducted at room temperature (298 K) and an initial pressure of 50 kPa. Prior to ignition, the mixture was left to settle to achieve quiescent conditions for one minute. Synchronisation was achieved via a purpose-written LabView program and a TTL signal to trigger the spark, camera and all data acquisition cards. The time separation between each experiment (> 20 min) and their short duration (< 100 ms) render (accumulative) preheating of the walls negligible and for modelling purposes boundary conditions can accordingly be treated as isothermal.

2.2. High speed particle image velocimetry

High speed (10 kHz) particle image velocimetry (HS-PIV) measurements were performed to determine the time-resolved development of the recirculation zone behind the second obstacle where the dominant explosion occurs. The interrogation region (IR) started 3 mm downstream of the obstacle. The HS-PIV system, controlled by LaVision DaVis 8.3, used the 2nd harmonic of an Edgeware Nd:YAG laser (IS6II-DE), a high speed camera (Photron Fastcam SA6) and an external LaVision high speed controller for synchronisation. The laser light sheet was directed vertically from the top of the flame tube into the optical section resulting in a thickness of around 0.8 mm in the centre of the recirculation zone. The camera was fitted with a 50 mm Nikon lens (f1.4) and a 3 nm narrow bandpass filter with a centre wavelength at 532 nm. Silicone fluid (Polycraft Dow Corning 200/50; flash point 373 K) was introduced as velocity tracer (seeding droplets) with an average number diameter of 0.5 μm using a liquid nebuliser (PALAS, AGF 10.0). Droplet evaporation at suitable seeding densities (< 10^{12} particles m^{-3}) has a negligible impact on the gas temperature (estimated < 1 K) and therefore on the expansion ratio across the flame front. The impact is further reduced by the heat released during combustion of the silicone fluid. A fused silica glass (268 (width) × 72 (height) × 25 mm (thickness)) was installed to provide optical access as shown in Figs. 1 and 2.

The time-resolved flow field was determined by means of adaptive PIV calculations in Davis 8.3 using normalised cross-correlation functions to compensate for the varying background and signal densities [37]. A multi-pass window shifting technique (128 × 128 to 32 × 32 pixels with 75% overlap) was used to minimise the out-of-pattern effect [38]. Adaptive shape modulation reduces the nominal interrogation region (IR) size in the direction of steep velocity gradients [39] and thereby improves the spatial resolution by up to a factor of 2 compared to conventional IRs at the penalty of longer calculation times [40]. Image pre-processing, i.e. background subtraction and dewarping, was performed prior
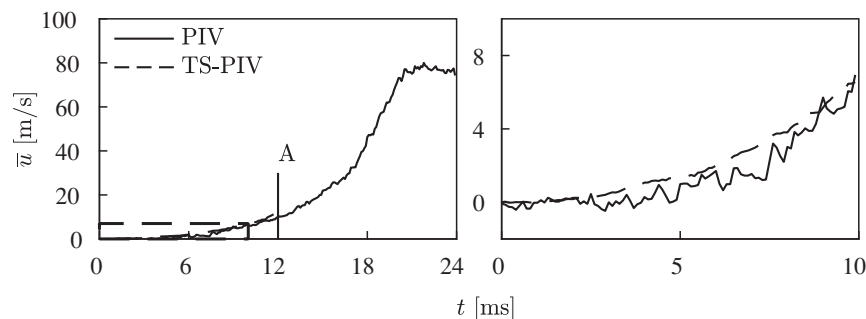

Fig. 3. Comparison of the standard and time-series PIV at a distance x = 10 mm downstream of the obstacle and at a height of y = 50 mm from the bottom of the flame tube in H_2/CO/Air mixtures with H_2 = 50% and $\Phi = 0.60$. The line A marks the transition velocity. The magnified figure on the right corresponds to the rectangle shown in the left panel.
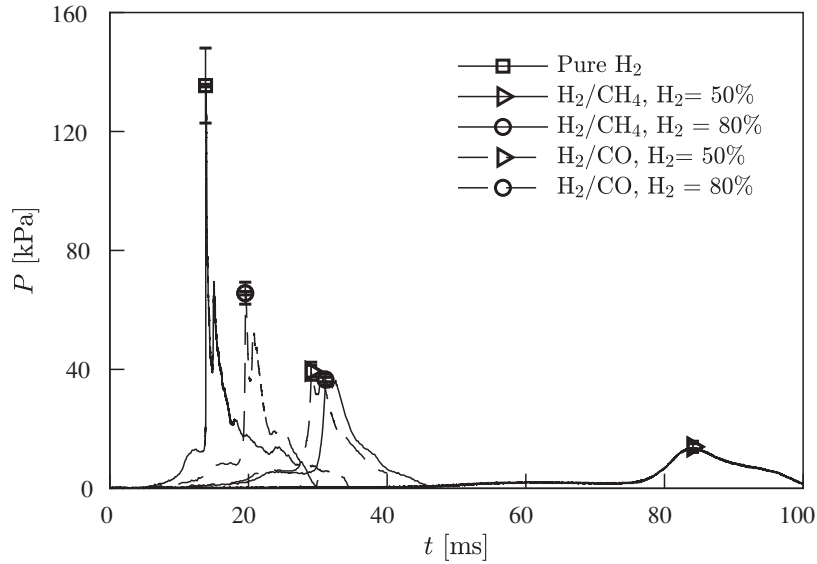
Fig. 4. Explosion over-pressure traces at the second pressure transducer located 1.305 m from the ignition end in $H_2/CH_4/Air$ and $H_2/CO/Air$ mixtures with $H_2 = 50$, 80 and 100% at $\Phi = 0.60$.
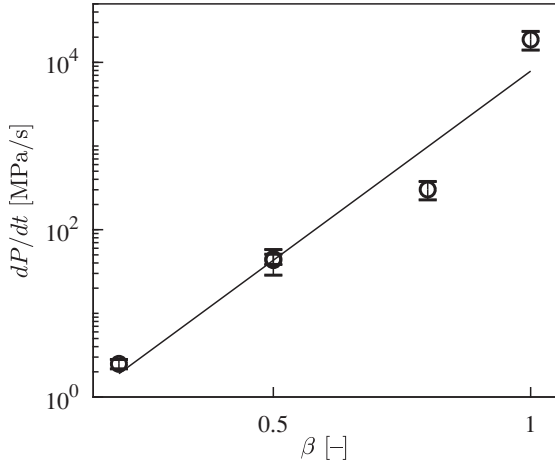

Fig. 5. Maximum pressure rise as a function of β derived from Fig. 4.

to the PIV calculations. The interrogation region featured a physical size of 52×63 mm that was resolved by 352×426 pixels. The resulting velocity field features 45×54 vectors with a spacing of 1.16 mm and an estimated spatial resolution of 2.35 mm (a maximum aspect ratio of 4 for the elliptical interrogation region). The timing between the double laser pulses (Δt) was optimised for the mixture reactivity dependent flow velocities as shown in Table 2. The transient flow necessitated velocity calculations to be performed using time-series PIV for low, and standard double-frame PIV for high, velocities due to the required pixel shift of seeding droplets between frames. The transition from time-series to double-frame PIV was found optimum when both methods provided the same mean velocity as shown in Fig. 3. The transition velocity was 12 m/s with a pulse separation $\Delta t = 15$ μs and 15 m/s for cases with a shorter Δt as listed in Table 2.

Li et al. [9] introduced the relationship shown in Eq. (1) ($0 \leq \beta \leq 1$) to scale a wide range of hydrogen enriched fuel blends with varying stoichiometric coefficients by defining the mixture composition based on the amount of air required to fully
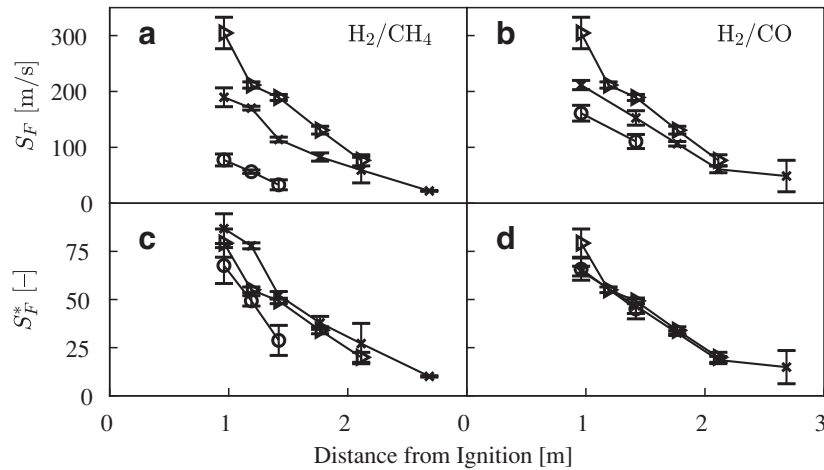

Fig. 6. Flame speeds in $H_2/CH_4/Air$ and $H_2/CO/Air$ mixtures with $H_2 = 50\%$ (○), 80% (×) and 100% (▷) and a stoichiometry of 0.60. The values of S_F are the measured flame speeds and $S_F^* = S_F/(\tau S_L)$ the normalised flame speeds where S_L and τ are the corresponding laminar burning velocities and expansion ratios (see Table 2).

Table 3

Summary of the characteristic results in the experiments where P_{max} is the peak over-pressure, FS_{max} the maximum flame speed obtained from the ionisation probes, u^+_{max} the maximum horizontal velocity in the free flow (y = 60 mm) and t_A the flame arrival time at the second obstacle.

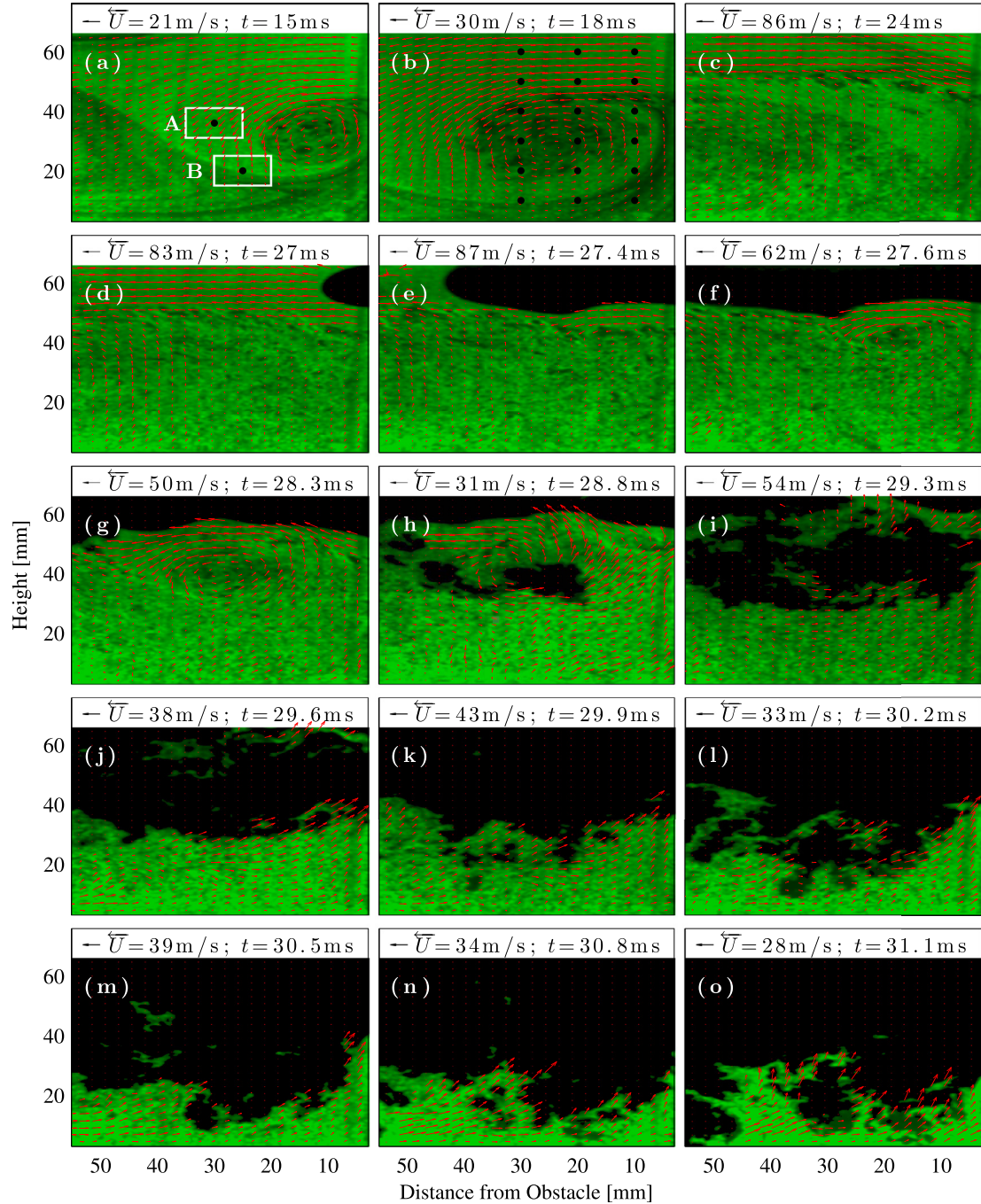| Mixture	H_2 %	β	P_{max} [kPa]	FS_{max} [m/s]	u^+_{max} [m/s]	t_A [ms]	dP/dt [MPa/s]
H_2	100	1.0	135 ± 13	305 ± 28	165 ± 6	11.5 ± 0.4	(19 ± 4.7) · 10^3
H_2/CH_4	50	0.20	14 ± 1	77 ± 11	29 ± 1	70 ± 2	2.5 ± 0.3
	80	0.50	37 ± 2	190 ± 17	76 ± 7	25 ± 0.6	45 ± 6.2
H_2/CO	50	0.50	39 ± 3	161 ± 15	79 ± 1	24 ± 0.3	43 ± 15
	80	0.80	66 ± 4	211 ± 8	111 ± 4	15.5 ± 0.5	302 ± 75

Fig. 7. High-speed (10 kHz) PIV and Mie scattering (green colour only) with superimposed velocity vectors at (a) 15 ms, (b) 18 ms, (c) 24 ms, (d) 27 ms, (e) 27.4 ms, (f) 27.6 ms, (g) 28.3 ms, (h) 28.8 ms, (i) 29.3 ms, (j) 29.6 ms, (k) 29.9 ms, (l) 30.2 ms, (m) 30.5 ms, (n) 30.8 ms and (o) 31.1 ms after ignition in a H_2/CH_4/Air mixture with H_2 = 80% and Φ = 0.60. The velocity vector length is scaled linearly with the velocity magnitude with the reference given at the top of each sub-graph. Areas A and B in (a) indicate the locations where a sensitivity analysis on the window size was performed. The dots in (b) show the grid points for which time-resolved velocity data are presented.
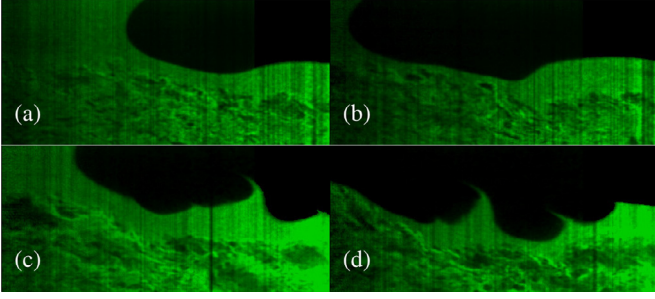
Fig. 8. Enhanced cusp formation associated with higher H_2 concentration. The flame front in a 80% H_2/20% CH_4 mixture at 27.3 and 27.5 ms after ignition is shown in (a) and (b) and that in a pure H_2 flame at 11.8 and 11.9 ms after ignition is illustrated in (c) and (d).
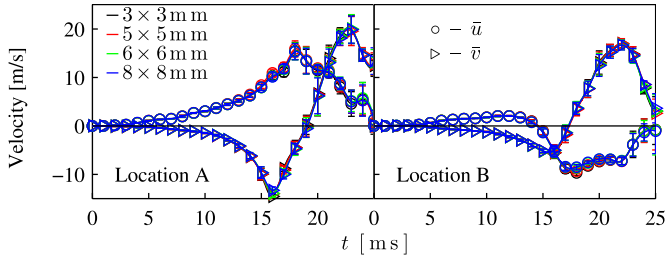

Fig. 9. Sensitivity of mean horizontal ($\bar{u}$) and vertical ($\bar{v}$) velocity components to window size (see Fig. 7a for the locations of windows A and B).

oxidise the fuel mixture.

$$\beta = \left[\frac{x_{H_2}}{(x_{H_2}/x_A)_{st}} \right] / \left[\frac{x_{H_2}}{(x_{H_2}/x_A)_{st}} + \sum_{k=1}^{n} \frac{x_{F,k}}{(x_F/x_A)_{st,k}} \right] \quad (1)$$

In Eq. (1), n is the number of fuel components, $x_{F,k}$ the mole fraction of the fuel component k (CO and/or CH_4) and $(x_F/x_A)_{st,k}$ the stoichiometric fuel to air mole fraction ratio for k, i.e. $(x_F/x_A)_{st,CH_4}$ = 0.105, $(x_F/x_A)_{st,CO}$ = 0.420 and $(x_F/x_A)_{st,H_2}$ = 0.420 with the mole fraction ratio $x_{N_2}/x_{O_2} \simeq 0.79/0.21$ for air. As shown in Table 2, the

H_2/CO/Air mixture with 50% H_2 and the H_2/CH_4/Air mixture with 80% H_2 have the same value of β and similarities in the flow field evolution are explored below.

2.3. PIV uncertainty estimation

The velocity lag between seeding particles and flow can introduce a systematic error in the measurement. The particle relaxation time (τ_p) to a step change in fluid velocity was estimated to be 0.74 µs using Eq. (2) [36,41], where d_p = 0.5 µm is the average number diameter of the seeding droplets, ρ_p is the silicone oil density (971 kg/m^3) and µ the reactant viscosity (see Table 2).

$$\tau_p = d_p^2 \frac{\rho_p}{18\mu} \quad (2)$$

The Kolmogorov time scale ($\tau_\eta \sim 10$ µs) was estimated via Eq. (3) based on a maximum bulk velocity of 200 m/s, a 10% turbulence intensity (u′) and a (maximum) integral length scale (L_I) corresponding to the obstacle height.

$$\tau_\eta \approx \frac{L_\eta^2}{\nu}, \quad L_\eta \approx \frac{L_I}{Re_t^{3/4}}, \quad Re_t \approx \frac{u' \cdot L_I}{\nu} \quad (3)$$

In the above, ν is the kinematic viscosity in the reactants and can be determined from ρ_0 and µ in Table 2. The frequency response [41] of the particles can resolve scales down to around 60 µm (or $3 \cdot L_\eta$). However, the smallest resolved scale by the current PIV technique was 2.35 mm. Thus, the seeding particles were sufficiently small to follow the resolved flow field with the Stokes number ($St = \tau_p/\tau_\eta \simeq 0.01$) well below unity. The estimation of τ_η depends on $L_I^{1/2}$ and division of L_I by a factor of 10 results in a Kolmogorov time scale of 4.2 µs and a Stokes number of 0.18.

Out-of-plane fluctuations may introduce errors in 2D PIV due to velocity bias and loss of seeding particles. Detailed analyses have been presented by Sinha [42] and Nishino et al. [43]. The maximum out-of-plane velocity was estimated to 20 m/s, based on a peak gas velocity of 200 m/s and assuming 10% fluctuations. The resulting out-of-plane particle displacement was ~ 0.1 mm (i.e. smaller than the light sheet thickness). The latter is a conservative estimate as the current geometry does not produce strong
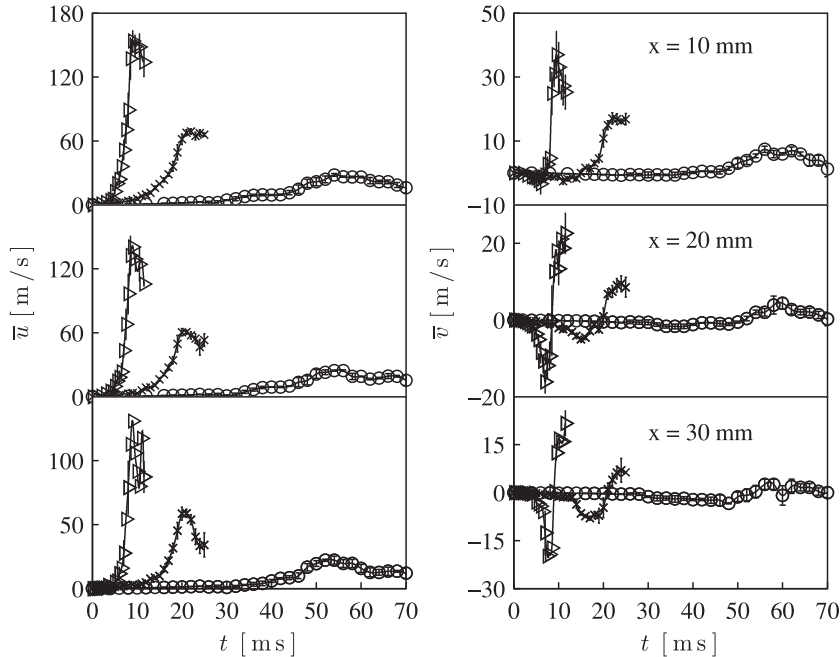

Fig. 10. Time-resolved velocities in H_2/CH_4/Air mixtures with H_2 = 50% ($\bigcirc$), 80% ($\times$) and 100% ($\triangleright$) along a horizontal line at a height (y) of 50 mm. Selected characteristic error bars are shown for clarity. Subplots correspond to distances from the obstacle (x) at 10, 20, 30 mm from top to bottom. Point locations refer to Fig. 7b.
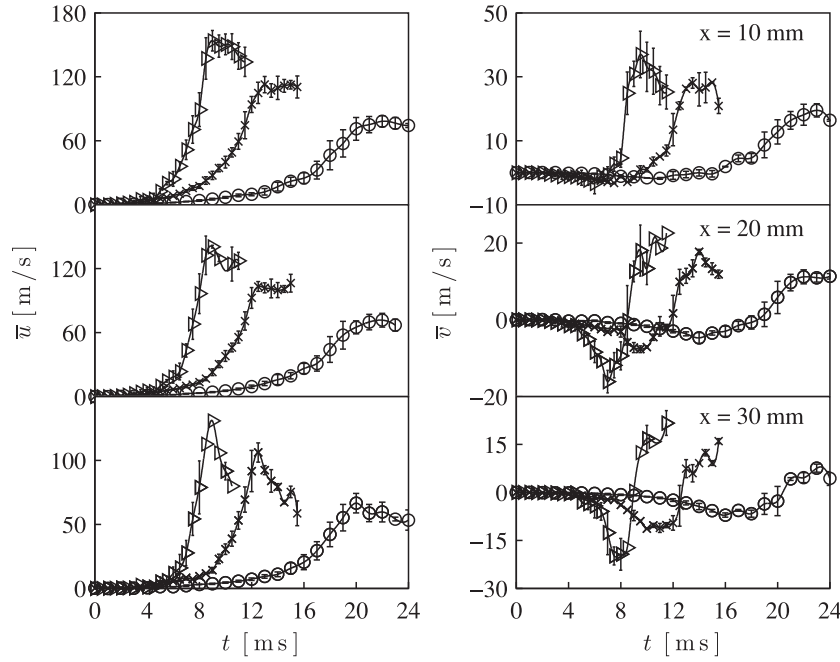
Fig. 11. Time-resolved velocities in $H_2/CO/Air$ mixtures with $H_2 = 50\%$ ($\bigcirc$), 80% ($\times$) and 100% ($\triangleright$) along a horizontal line at a height (y) of 50 mm. Selected characteristic error bars are shown for clarity. Subplots correspond to distances from the obstacle (x) at 10, 20, 30 mm from top to bottom. Point locations refer to Fig. 7b.

cross flows. The velocity bias error due to spurious displacement [42,43] was below 0.1%.

Strong heat release in thin reaction layers and corresponding temperature gradients can lead to uncertainties associated with thermophoresis and beam steering [44,45]. In laboratory scale facilities the latter is negligible for sufficiently small PIV pulse separations [44] as used in the current study. The impact of thermophoresis was also insignificant as the measurements were performed in the reactants ahead of the flame front and the silicone oil seeding particles evaporate at a temperature of 373 K.

3. Results and discussion

The data is first analysed in terms of peak over-pressures and flame speeds in Section 3.1 and subsequently for the associated flow fields in Sections 3.2–3.3.

3.1. Pressure development and flame speed

The rate of heat release is greatly enhanced by turbulence in the developing recirculation zones behind the obstacles. The timing and magnitude of the pressure peaks caused by the resulting fast deflagrations are strongly dependent on the mixture reactivity. Figure 4 illustrates the pressure development in $H_2/CH_4/Air$ and $H_2/CO/Air$ mixtures with different hydrogen substitutions. The over-pressures ($P^* = P/P_0$, where $P_0 = 50$ kPa is the initial pressure) were obtained from the second pressure transducer located at a distance of 1.305 m from the ignition end and correspond approximately to the maximum recorded in the absence of pressure waves reflected from the non-ignition end. The peak pressure originates from the volumetric consumption of the highly turbulent recirculation zone in the wake of the (final) second obstacle [9].

A change in the hydrogen concentration impacts the peak over-pressure differently for CH_4 and CO mixtures. The peak pressure for $H_2/CH_4/Air$ mixtures is strongly non-linear with an increase by

a factor of two moving from 50% to 80% and a factor of three from 80% to 100% hydrogen content. By contrast, the $H_2/CO/Air$ mixtures show an increase close to a factor of two moving from 50% to 80% and then to 100% H_2 substitution. Furthermore, at a given hydrogen substitution, the $H_2/CO/Air$ mixtures give higher peak over-pressures and a faster flame propagation, suggesting a stronger inhibiting effect of CH_4 than CO. These findings are consistent with the data presented by Li et al. [9]. Furthermore, it can be noted that the $H_2/CH_4/Air$ mixture with 80% H_2 and $H_2/CO/Air$ with 50% H_2 share the same value $\beta = 0.50$ and show a similarity in terms of the magnitude of the peak pressure and the temporal evolution. The maximum temporal pressure gradient (dP/dt) was determined for each experiment using the traces recorded at the second pressure transducer and is shown as a function of β in Fig. 5. The dP/dt for the 100% H_2 mixture is ~ 7500 times higher than for the $H_2/CH_4/Air$ mixture with 50% H_2 and 62 times higher than the $H_2/CO/Air$ mixture with 80% H_2. The two mixture with $\beta = 0.5$ (i.e. 80% $H_2/CH_4/Air$ and 50% $H_2/CO/Air$) show very similar relative pressure rises of 45 and 43 MPa/s, see Table 3.

Flame speeds (S_F), inferred from flame arrival time measurements as detailed by Li et al. [9], are shown in the top two panels in Fig. 6. The flame speed decreases with a reduction in hydrogen content due to the reduced mixture reactivity. The decay of the explosion results in reduced flame speeds with increasing distance as DDT is not recorded. The variations in S_F are related to the flame development, including (stochastic) interactions with the evolving recirculation eddy, and initial conditions. The variability is below 10% ($< 15\%$ for the 50/50 H_2/CH_4 mixture) which suggests good experimental repeatability. The stronger inhibiting effect of CH_4 is reflected in the reduced flame speed at the same level of hydrogen enrichment. The lower two panels show the dimensionless flame speeds normalised by the product of the laminar burning velocity and expansion ratio (see Table 2), i.e. $S_F^* = S_F/(\tau S_L)$. It is evident that for the current data sets the impact of mixture reactivity on the flame propagation speed can be scaled reasonably well using this approach.
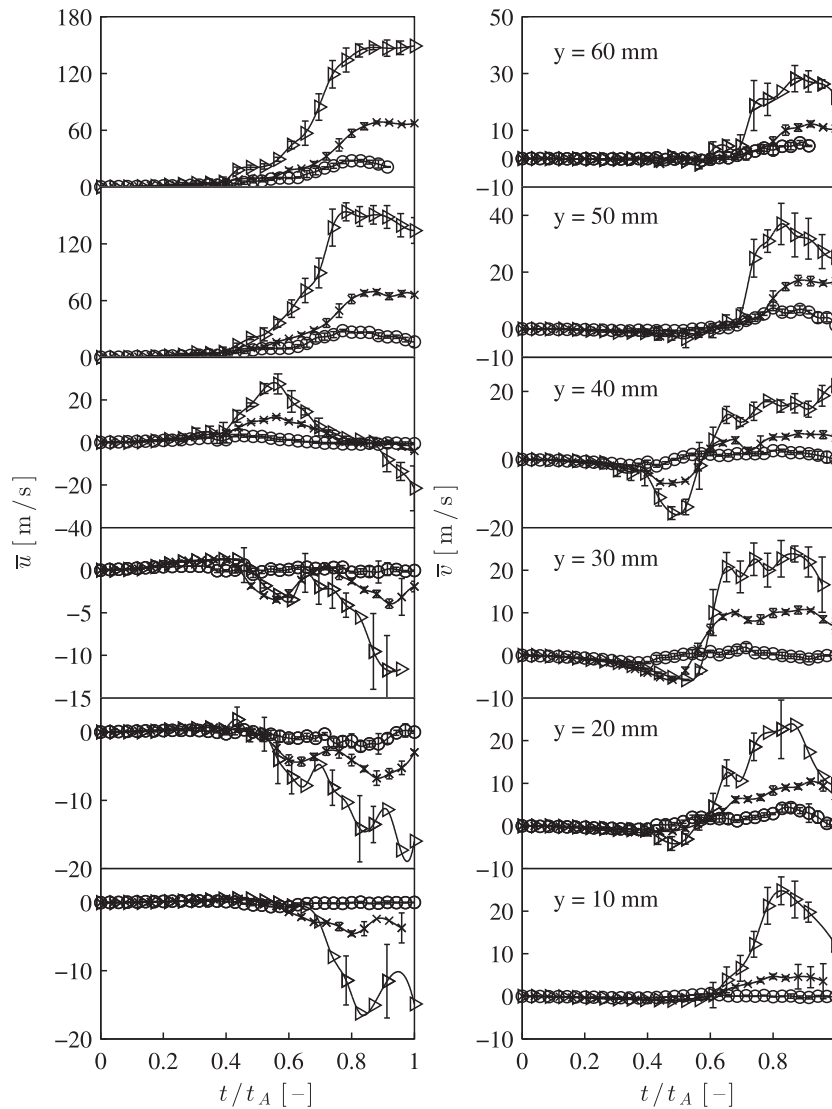
Fig. 12. Normalised (t/t_A) time-resolved velocities in H_2/CH_4/Air mixtures with $H_2 = 50\%$ ($\bigcirc$), 80% ($\times$) and 100% ($\triangleright$) at $x = 10$ mm downstream of the obstacle. Selected characteristic error bars are shown for clarity. Subplots correspond to heights (y) at 60, 50, 40, 30, 20, 10 mm from top to bottom. Point locations refer to Fig. 7b.

3.2. Flow and flame front visualisation

High speed PIV at 10 kHz was performed to quantify the flow evolution in the recirculation zone behind the second obstacle where the dominant explosion occurs. The time-series in Fig. 7 shows every three milliseconds of the developing flow pattern ahead of the flame front for a H_2/CH_4/Air mixture with 80% H_2. The Mie scattering (green/light colour) images are superimposed on the PIV velocity vectors. The black parts signify the flame arrival and an absence of silicone oil droplets (evaporation temperature of 373 K). The eddy continuously grows with the centre moving downstream away from the obstacle, particularly prominent in the time windows up to 24 ms. A maximum velocity of around 90 m/s was observed for this mixture just prior to the flame arrival in the interrogation region. The reactants in the recirculation zone were subsequently rapidly consumed via a highly fragmented flame front, as shown in panels (h) to (o), with islands of combustion products surrounded by reactants. The peak pressure also occurred at around 30 ms and highlights the correlation with the turbulent explosion in the recirculation zone behind the second obstacle.

Flame instabilities in explosions have been studied extensively by Bradley et al. [46–48] and cusps are observed in the current pure hydrogen flames with cold gas penetrating vertically into the combustion products as shown in Fig. 8. By contrast, for the fuel blends the flame fronts remain relatively smooth as also shown. The temporal pressure gradient shown in Fig. 5 is nearly two orders of magnitude higher for the 100% H_2 mixture than for the CO fuel blend with 80% H_2. The cusp formation shown in Fig. 8 suggests that flame instabilities contributed to the strength of the explosion. Similar disturbances of the flame front were also observed for stoichiometric methane flames using Schlieren photography by Sakthitharan [33] and attributed to Rayleigh-Taylor instabilities caused by interactions between the accelerating flow field and the density difference across the flame front. Large scale experiments [48] further show that spherically expanding flames become unstable above a critical Peclet number that depends on the Markstein number. Law et al. [49] investigated cellular instabilities of expanding spherical flames using hydrogen/propane mixtures with instabilities correlating with an increase in H_2 concentration at $\Phi = 0.80$ and attributed to the reduced flame thickness. The effect of equivalence ratio was also assessed using
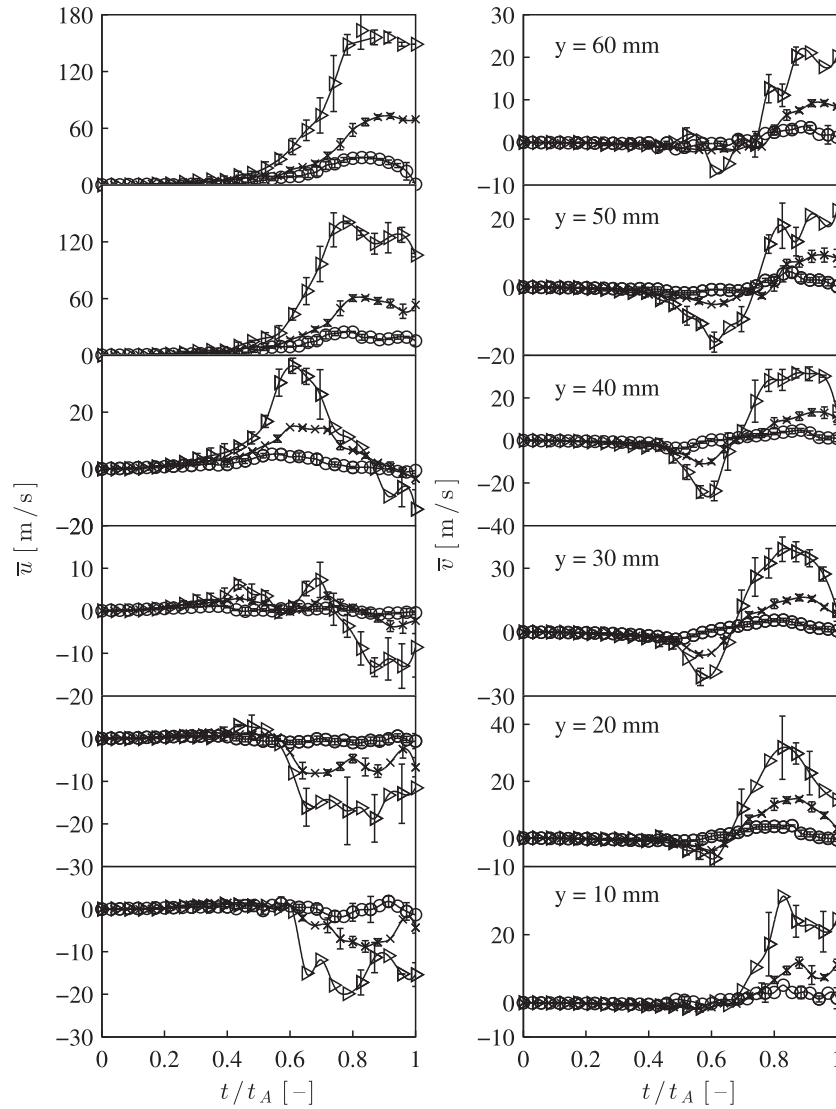
Fig. 13. Normalised (t/t_A) time-resolved velocities in $H_2/CH_4/Air$ mixtures with $H_2 = 50\%$ ($\bigcirc$), 80% ($\times$) and 100% ($\triangleright$) at x = 20 mm downstream of the obstacle. Selected characteristic error bars are shown for clarity. Subplots correspond to heights (y) at 60, 50, 40, 30, 20, 10 mm from top to bottom. Point locations refer to Fig. 7b.

mixtures with Φ = 0.60, 1.00 and 1.40 with leaner mixtures more prone to destabilise. Moccia and D'Alessio [50] studied spherically expanding flames in stoichiometric CH_4/H_2 mixtures with 10%, 20% and 30% H_2 at elevated initial pressures (3, 6 and 12 bar). An earlier onset of the cellular structure was observed with increased H_2 fractions. For the fuel lean mixtures in the current experimental configuration, instabilities at the interface between reactants and products contribute to the rapid breakup of the initially laminar flame structure at H_2 levels $\geq 80\%$.

3.3. Flow field evolution

The time-resolved flow evolution in the recirculation zone was quantified by means of mean horizontal ($\bar{u}$) and vertical ($\bar{v}$) velocity components at 18 equally spaced discrete points. A median filter was used in the time domain to reduce the impact of outliers. The locations of the points are shown in Fig. 7b with horizontal distances of 10, 20, 30 mm from the obstacle and heights of 60, 50, 40, 30, 20, 10 mm. The average was determined using square interrogation windows centred at the discrete points. A sensitivity analysis on the window size (3 × 3, 5 × 5, 6 × 6 and 8 × 8 mm) was

performed at two characteristic positions A and B (see Fig. 7a) with negligible differences as shown in Fig. 9. Thus, the subsequent data analysis uses a 5 × 5 mm window size containing around 20 vectors. Figures 10 and 11 show the flow field development in H_2/CH_4 and H_2/CO mixtures, respectively, at three locations at the same height (y = 50 mm), but at different distances from the obstacle (x = 10, 20, 30 mm). The use of a dimensionless time ($t^* = t/t_A$, where t_A is the flame arrival time at the second obstacle as listed in Table 3), eases the comparison of the flow field development for mixtures with different reactivities. Figures 12–14 show the mean horizontal ($\bar{u}$) and vertical ($\bar{v}$) velocities for the $H_2/CH_4/Air$ mixtures at points 10, 20, 30 mm downstream from the second obstacle in the normalised time domain. The results for the $H_2/CO/Air$ mixtures are depicted in Figs. 15–17. The subplots in each figure correspond to the points at heights 60, 50, 40, 30, 20, 10 mm, i.e. from the top towards the bottom.

3.3.1. Impact of mixture reactivity

The velocity development shows a qualitative similarity in the normalised time domain for all mixtures. The maximum positive horizontal velocity (u_{max}^+ for flow away from the obstacle) is
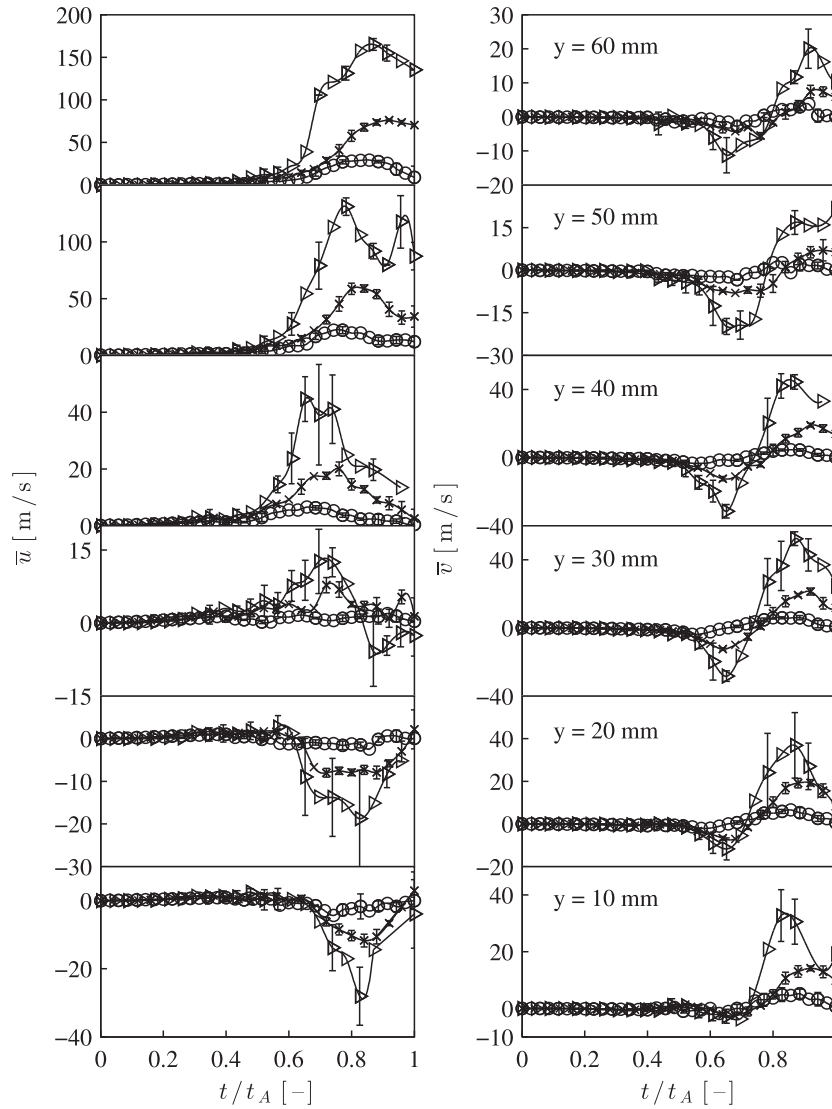
Fig. 14. Normalised (t/t_A) time-resolved velocities in $H_2/CH_4/Air$ mixtures with $H_2 = 50\%$ ($\bigcirc$), 80% ($\times$) and 100% ($\triangleright$) at x = 30 mm downstream of the obstacle. Selected characteristic error bars are shown for clarity. Subplots correspond to heights (y) at 60, 50, 40, 30, 20, 10 mm from top to bottom. Point locations refer to Fig. 7b.

consistently found in the free flow (i.e. y = 60 mm) and increases with mixture reactivity. Specifically, in CH_4/H_2 mixtures, u^+_{max} increases from 29, 76 to 165 m/s when moving from 50%, 80% to pure hydrogen while for CO/H_2 mixtures, it increases from 79, 111 to 165 m/s (see Table 3). This also shows the stronger inhibiting effect of CH_4 compared to CO and correlates well with the explosion over-pressure (see Section 3.1). The two mixtures with $\beta = 0.50$ ($H_2/CH_4/Air$ with $H_2 = 80\%$ and $H_2/CO/Air$ with $H_2 = 50\%$) show distinct similarities in measured parameters. Figure 18 exemplifies the time-resolved velocity evolution in the two mixtures at location x = 10 mm, y = 50 mm. The maximum reverse flow towards the obstacle (i.e. negative horizontal component, u^-_{max}) for all mixtures is found at the bottom of the tube, i.e. y = 10 mm, with a maximum value of around −19 m/s in the pure H_2 mixture – around eightfold (twofold) of that in 50% CH_4 (CO) fuel blend mixture. The vertical velocity component is mainly induced by the downstream motion of the recirculation eddy and the maximum vertical velocity components in positive (v^+_{max}) and negative (v^-_{max}) directions are found close to the centre of the tube (i.e. y = 30 or 40 mm) as expected. Both v^+_{max} and v^-_{max} in pure hydrogen

mixture are around sevenfold and twofold of that in 50% CH_4 and 50% CO mixtures, respectively. Therefore, the strength of the recirculation eddy increases significantly with mixture reactivity. For each mixture v^+_{max} is larger than v^-_{max}, indicating an asymmetrical structure of the recirculation eddy imposed by the obstacle and free flow [26].

3.3.2. Impact of distance from the obstacle

The maximum horizontal velocity component (u^+_{max}) in the free flow region at y = 60 mm increases by approximately 11% with distance from the obstacle (i.e. x = 10–30 mm). By contrast, u^+_{max} at y = 50 mm reduces by $\sim 14\%$ with increasing distance for all mixtures. The value of u^+_{max} decreases substantially with distance from the top of the flame tube as shown in Figs. 12–17. At y = 30 mm, the values of u^+_{max} reduce to around 5% of that in the free stream region (y = 60 mm) for all mixtures. This indicates the existence of a strong shear layer with associated turbulence generation at the height of the obstacle. The horizontal component becomes negative close to the bottom due to the flow reversal caused by recirculation and u^-_{max} increases with decreasing in the distance to the
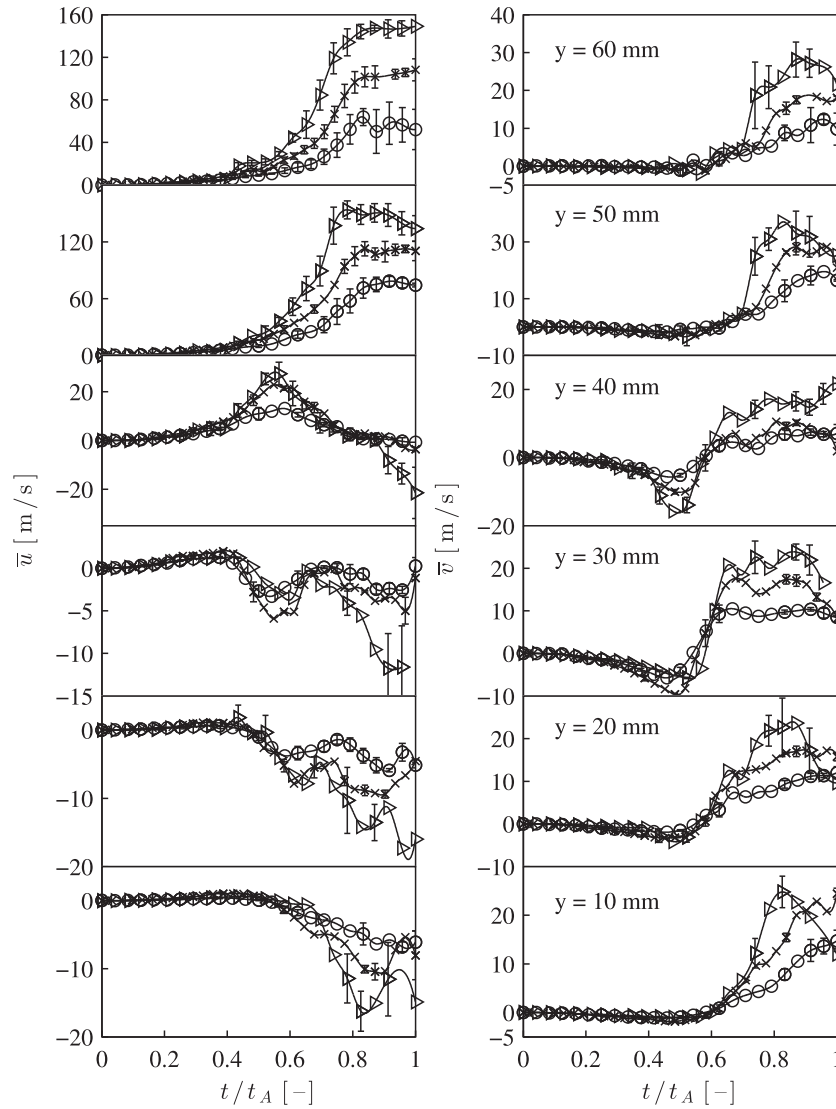
Fig. 15. Normalised (t/t_A) time-resolved velocities in H_2/CO/Air mixtures with H_2 = 50% (○), 80% (×) and 100% (▷) at x = 10 mm downstream of the obstacle. Selected characteristic error bars are shown for clarity. Subplots correspond to heights (y) at 60, 50, 40, 30, 20, 10 mm from top to bottom. Point locations refer to Fig. 7b.

bottom. Specifically, at distances of 10 and 20 mm downstream, $\bar{u}$ becomes negative below 30 mm in height, while at 30 mm downstream, it becomes negative only below 20 mm in height. Consequently, the recirculation zone is compressed towards the bottom of the tube with increasing distance. The $\bar{v}$ component is generally negative first in the middle of the tube (20 < y < 50 mm) before turning positive. The maximum magnitude (v_{max}^+ and v_{max}^-) are of similar magnitude in the range 20–40 m/s. This corresponds well with LDA data [26] for stoichiometric CH_4/air mixtures. Thus, the flow evolution in the recirculation zone is qualitatively similar for the different mixtures, but with strong variations in velocity magnitudes.

3.3.3. Recirculation zone development

The movement of the centre of the recirculation eddy formed behind the second obstacle was tracked and the translation velocity in the horizontal direction ($\bar{u}$) calculated. Therefore, the eddy centre was defined as the minimum of the velocity magnitude (i.e. $min(|u_i|) = 0$), see Eq (4).

$$|u_i| = (u_i^2 + v_i^2)^{1/2}$$
$$\mathbf{x}_i = \mathbf{x}|min(|u_i|)$$
$$\bar{u} = \frac{\mathbf{x}_{i+1} - \mathbf{x}_i}{\Delta t} \tag{4}$$

Linear interpolation of the nearest positive and negative vector pair of the velocity components (u_i, v_i) allowed the accurate determination of position of the absolute minimum. The eddy centre position (x) at time i was determined by the location of $min(|u_i|)$. Subsequently, the translation velocity was calculated from the displacement of the eddy centre (x_i) over the time period ($\Delta t = t_{i+1} - t_i$) between frames. The eddy was tracked through the PIV interrogation window starting from 3 to 30 mm behind the second obstacle. The maximum uncertainty of the eddy centre location is the vector spacing (i.e. ∼1.16 mm), which results in maximum uncertainties in the translation velocities of (i) 3.9, (ii) 2.3 and (iii) 0.58 m/s for (i) pure H_2, (ii) H_2/CH_4 with H_2 = 80%, H_2/CO with H_2 = 50% and 80% and (iii) H_2/CH_4 with H_2 = 50%, respectively. The eddy translation velocity increases with time due to the
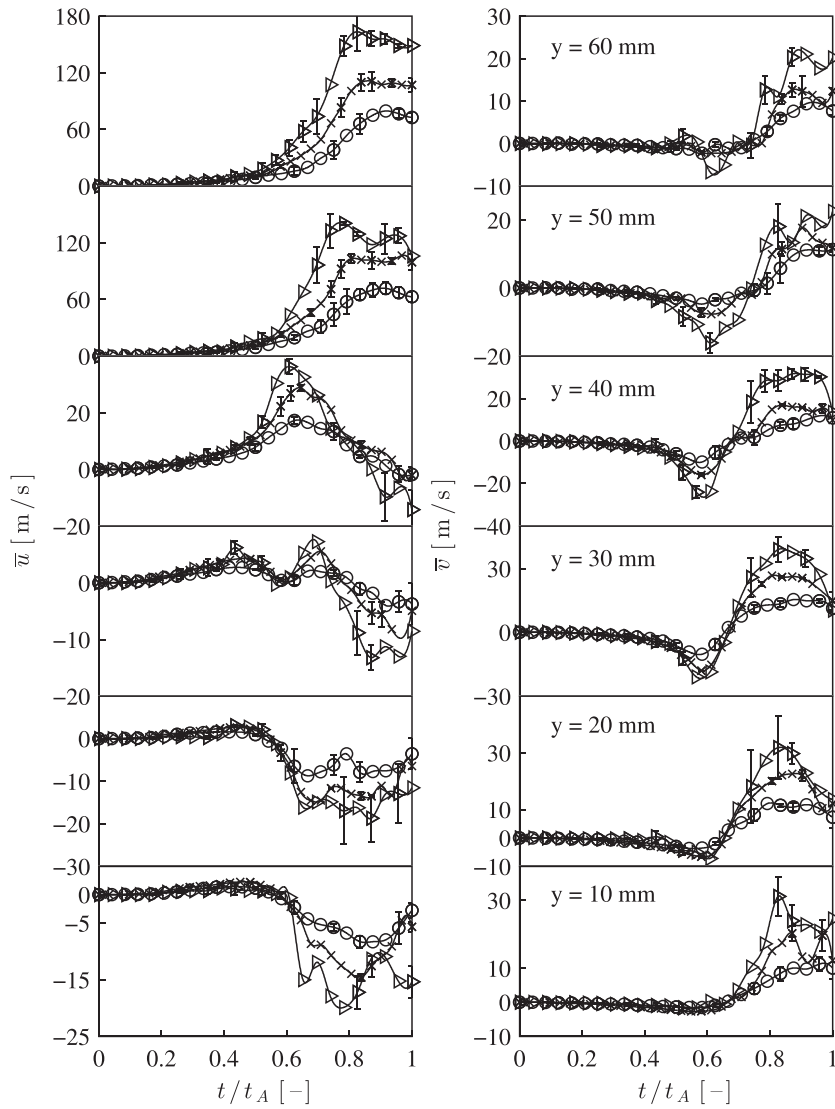
Fig. 16. Normalised (t/t_A) time-resolved velocities in $H_2/CO/Air$ mixtures with $H_2 = 50\%$ (◯), 80% ($\times$) and 100% (▷) at x = 20 mm downstream of the obstacle. Selected characteristic error bars are shown for clarity. Subplots correspond to heights (y) at 60, 50, 40, 30, 20, 10 mm from top to bottom. Point locations refer to Fig. 7b.

progressive flow acceleration ahead of the flame front as shown in Fig. 19. The bars show the variations between different experiments. The translation velocity increases with hydrogen concentration with the maximum in the pure hydrogen mixture is around four times that of the 50% CH_4 fuel blend. The 50% CO fuel blend shows a reduction in the translation velocity of a factor of three. As discussed in Section 3.3.1, the two mixtures with $\beta = 0.50$ ($H_2/CH_4/Air$ with $H_2 = 80\%$ and $H_2/CO/Air$ with $H_2 = 50\%$) show distinct similarities in the flow field development that is also apparent in the eddy development time and translation velocity (S_E) as depicted in Fig. 19. The H_2/CO data were truncated due to a deteriorating image quality far away from the obstacle.

The recirculation eddy is the result of the thermal expansion of the combustion products during the initial flame development. The flame front is relatively smooth leading up to the obstacle, see Figs. 7 and 8, and the rate of thermal expansion can be scaled approximately by the product of the laminar burning velocity and expansion ratio. The horizontal translation velocity of the eddy centre normalised this way (S_E^*) is shown in Fig. 20. The time is normalised by t_A (see Table 3), where $t/t_A = 0$ and 1 is the ignition and flame arrival time in the PIV interrogation region, respectively. The suggested normalisations provide some correlation of the data. The fitted line in Fig. 20 considers the entire data set and has been introduced for guidance.
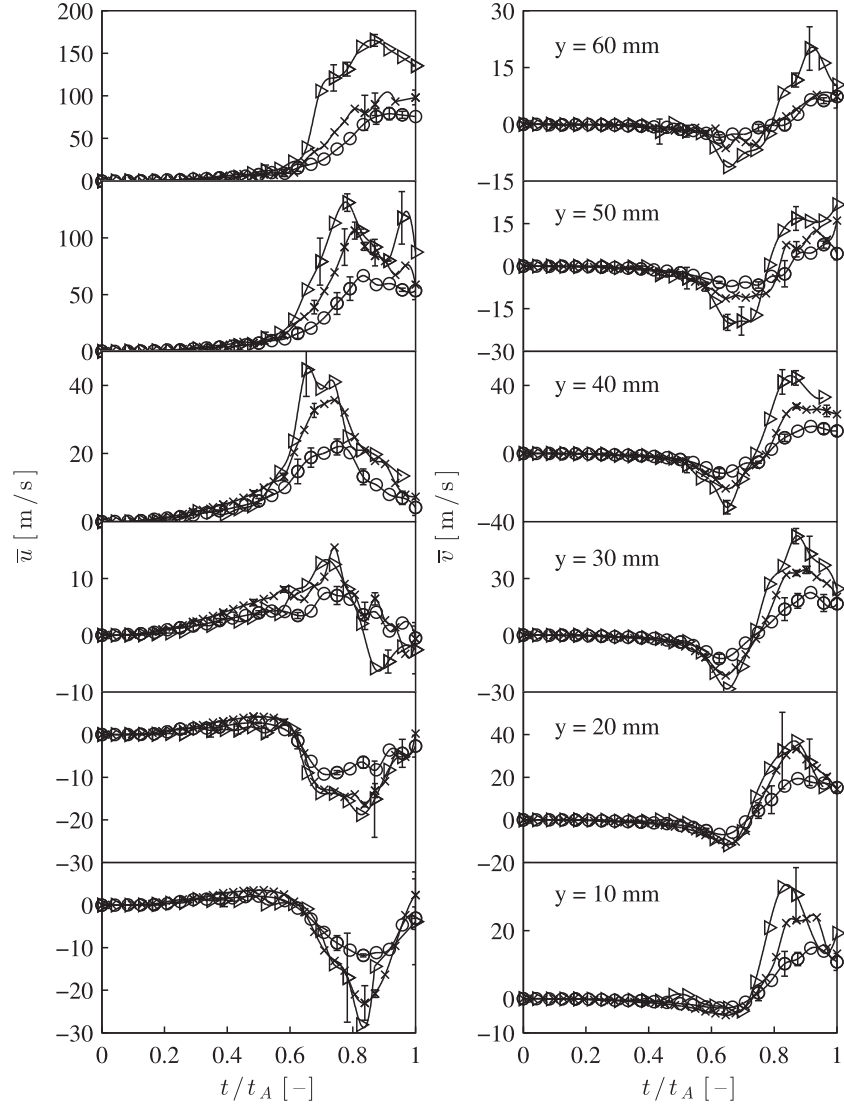
Fig. 17. Normalised (t/t_A) time-resolved velocities in $H_2/CO/Air$ mixtures with $H_2 = 50\%$ ($\bigcirc$), 80% ($\times$) and 100% ($\triangleright$) at x = 30 mm downstream of the obstacle. Selected characteristic error bars are shown for clarity. Subplots correspond to heights (y) at 60, 50, 40, 30, 20, 10 mm from top to bottom. Point locations refer to Fig. 7b.
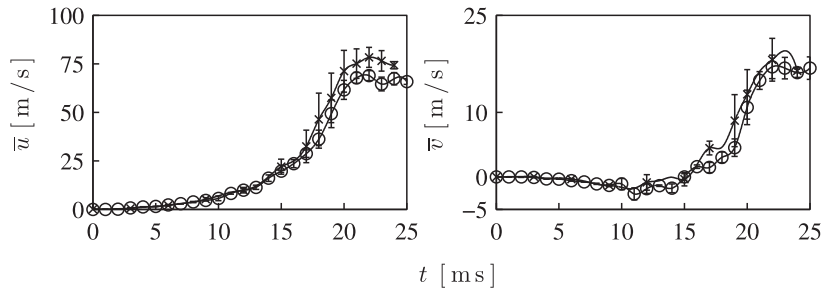

Fig. 18. Time-resolved velocities in $H_2/CH_4/Air$ with $H_2 = 80\%$ ($\bigcirc$) and $H_2/CO/Air$ with $H_2 = 50\%$ ($\times$) mixtures sharing the same $\beta = 0.50$ at location x = 10 mm, y = 50 mm (refer to Fig. 7b.)

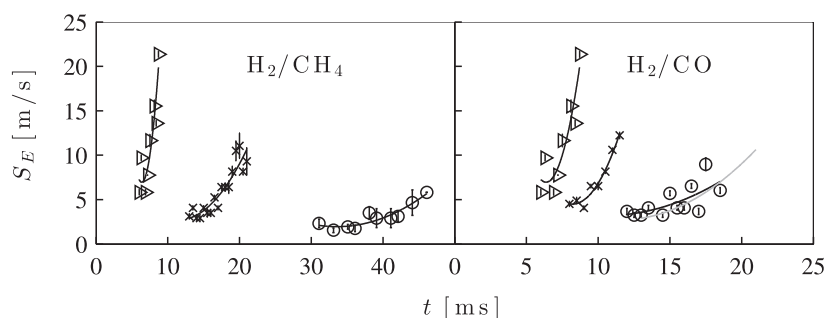**Fig. 19.** The horizontal translation velocity of the eddy centre in H_2/CH_4/Air and H_2/CO/Air mixtures with $H_2 = 50\%$ ($\bigcirc$), 80% ($\times$) and 100% ($\triangleright$). The grey line in the right panel is a fit for H_2/CH_4/Air with $H_2 = 80\%$ shown for β comparisons.
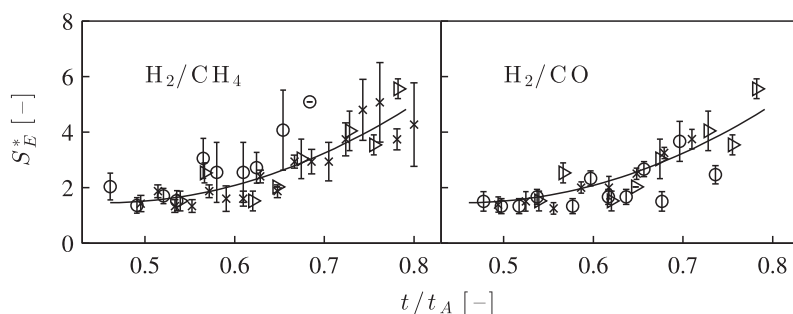

Fig. 20. The horizontal translation velocity of the eddy centre normalised by the laminar burning velocity and the expansion ratio. Symbols as in Fig. 19. The time is normalised by the flame arrival time (t_A) in the interrogation region. The polynomial is fittet to the entire data set to guide the eye.

4. Conclusions

Turbulent explosions resulting from fuel lean hydrogen enriched CH_4/Air and CO/Air mixtures at an initial pressure of 50 kPa and room temperature were experimentally studied in an obstructed flame tube. High-speed PIV measurement at 10 kHz were performed in the critical recirculation region behind the second obstacle to assess the impact of the mixture reactivity on the evolution of the resulting explosion. Over-pressures and flame speeds were also measured. The mixture reactivity was modified by introducing different hydrogen substitutions (50, 80 and 100%) at a fixed stoichiometry of 0.60. A stronger inhibiting effect of CH_4 on the chemistry of H_2 was observed to the point where $80\%H_2/20\%CH_4$/Air and $50\%H_2/50\%CO$/Air mixtures showed significant similarities in flow field development. Both mixtures share the same value $\beta = 0.5$ of the scaling parameter introduced by Li et al. [9] to correlate explosion over-pressures in syngas related fuel blends. The flame morphology during the propagation was visualised with Mie scattering and the centre of the shear driven recirculation eddy was tracked with the horizontal translation velocity calculated and results shown to be consistent with the β scaling. The flow field was further quantified by determining the mean horizontal ($\bar{u}$) and vertical ($\bar{v}$) velocity components via combined PIV and time-series PIV for an equally spaced matrix with 18 discrete points per mixture. The contribution of the $\bar{u}$ and $\bar{v}$ components to the overall velocity magnitude was quantified along with differences in the flame propagation caused by the mixture reactivity. It was shown that normalisation with the flame arrival time at the second obstacle, where the dominant explosion occurs, provided a convenient means of comparing the time evolution of the velocity fields. Further normalisation using the product of the thermal expansion ratio and laminar burning velocity was found to improve the correlation of the measured flame speed data. The current data sets provide a comprehensive quantification of the time-resolved flow evolution in the

recirculation zone ahead of the advancing flame front and quantifies the link between fuel reactivity and the flow field, flame acceleration and resulting over-pressures. The database is expected to support the further development of models for turbulent explosions.

Supplementary material

Tabulated data in spreadsheet format associated with this article can be found in the supplemental material. Supplementary material associated with this article can be found, in the online version, at doi:10.1016/j.combustflame.2019.01.037.

References

[1] B. Korb, S. Kawauchi, G. Wachtmeister, Influence of hydrogen addition on the operating range, emissions and efficiency in lean burn natural gas engines at high specific loads, Fuel 164 (2016) 410–418.

[2] B. Zhang, C. Ji, S. Wang, Performance of a hydrogen-enriched ethanol engine at unthrottled and lean conditions, Energ. Convers. Manag. 114 (2016) 68–74.

[3] F. Amrouche, P.A. Erickson, J.W. Park, S. Varnhagen, An experimental evaluation of ultra-lean burn capability of a hydrogen-enriched ethanol-fuelled wankel engine at full load condition, Int. J. Hydrogen Energ. 41 (2016) 19231–19242.

[4] J.H.S. Lee, R. Knystautas, A. Freiman, High speed turbulent deflagrations and transition to detonation in H_2–air mixtures, Combust. Flame 56 (1984) 227–239.

[5] F. Cammarota, A.D. Benedetto, V.D. Sarli, E. Salzano, G. Russo, Combined effects of initial pressure and turbulence on explosions of hydrogen-enriched methane/air mixtures, J. Loss Prevent. Proc. 22 (2009) 607–613.

[6] E. Salzano, F. Cammarota, A.D. Benedetto, V.D. Sarli, Explosion behavior of hydrogen-methane/air mixtures, J. Loss Prevent. Proc. 25 (2012) 443–447.

[7] B.J. Lowesmith, C. Mumby, G. Hankinson, J.S. Puttock, Vented confined explosions involving methane/hydrogen mixtures, Int. J. Hydrogen Energ. 36 (2011) 2337–2343.

[8] M. Schiavetti, M. Carcassi, Maximum overpressure vs. H_2 concentration non–monotonic behavior in vented deflagration. experimental results, Int. J. Hydrogen Energ. 42 (2017) 7494–7503.

[9] T. Li, F. Hampp, R.P. Lindstedt, Turbulent explosions in hydrogen enriched syngas related fuel blends, Process Saf. Environ. 116(2018) 663–676.

[10] C.R. Bauwens, J. Chaffee, S.B. Dorofeev, Vented explosion overpressures from combustion of hydrogen and hydrocarbon mixtures, Int. J. Hydrogen Energ. 36 (2011) 2329–2336.

[11] C.R. Bauwens, J. Chao, S.B. Dorofeev, Effect of hydrogen concentration on vented explosion overpressures from lean hydrogen–air deflagrations, Int. J. Hydrogen Energ. 37 (2012) 17599–17605.

[12] D. Bradley, M. Lawes, M.S. Mansour, The problems of the turbulent burning velocity, Flow Turbul. Combust. 87 (2011) 191–204.

[13] D. Bradley, M. Lawes, M.S. Mansour, Measurement of turbulent burning velocities in implosions at high pressures, Proc. Combust. Inst. 33 (2011) 1269–1275.

[14] D. Bradley, M. Lawes, K. Liu, M.S. Mansour, Measurements and correlations of turbulent burning velocities over wide ranges of fuels and elevated pressures, Proc. Combust. Inst. 34 (2013) 1519–1526.

[15] I.O. Moen, M. Donato, R. Knystautas, J.H. Lee, Flame acceleration due to turbulence produced by obstacles, Combust. Flame 39 (1980) 21–32.

[16] R.P. Lindstedt, H.J. Michels, Deflagration to detonation transitions and strong deflagrations in alkane and alkene air mixtures, Combust. Flame 76 (1989) 169–181.

[17] S.S. Ibrahim, A.R. Masri, The effects of obstructions on overpressure resulting from premixed flame deflagration, J. Loss Prevent. Proc. 14 (2001) 213–221.

[18] A.M. Na'inna, H.N. Phylaktou, G.E. Andrews, The acceleration of flames in tube explosions with two obstacles as a function of the obstacle separation distance, J. Loss Prevent. Proc. 26 (2013) 1597–1603.

[19] V.N. Gamezo, T. Ogawa, E.S. Oran, Flame acceleration and DDT in channels with obstacles: effect of obstacle spacing, Combust. Flame 155 (2008) 302–315.

[20] D. Bradley, M. Lawes, K. Liu, Turbulent flame speeds in ducts and the deflagration/detonation transition, Combust. Flame 154 (2008) 96–108.

[21] G. Ciccarelli, C.T. Johansen, M. Parravani, The role of shock-flame interactions on flame acceleration in an obstacle laden channel, Combust. Flame 157 (2010) 2125–2136.

[22] T. Ogawa, V.N. Gamezo, E.S. Oran, Flame acceleration and transition to detonation in an array of square obstacles, J. Loss Prevent. Proc. 26 (2013) 355–362.

[23] C. Chan, I.O. Moen, J.H.S. Lee, Influence of confinement on flame acceleration due to repeated obstacles, Combust. Flame 49 (1983) 27–39.

[24] G. Ciccarelli, S. Dorofeev, Flame acceleration and transition to detonation in ducts, Prog. Energ. Combust. 34 (2008) 499–550.

[25] C. Johansen, G. Ciccarelli, Characterization of the flow field ahead of a flame propagating in an obstructed channel, 24th International Colloquium on the Dynamics of Explosion and Reactive Systems, Poitiers, France (2007). Paper 0242

[26] R.P. Lindstedt, V. Sakthitharan, Time resolved velocity and turbulence measurements in turbulent gaseous explosions, Combust. Flame 114 (1998) 469–483.

[27] F. Hampp, R.P. Lindstedt, Fractal grid generated turbulence - a bridge to practical combustion applications, in: Y. Sakai, C. Vassilicos (Eds.), Fractal Flow Design: How to Design Bespoke Turbulence and why, Springer-Verlag (2016). CISM Int. Mech. Sci. 568, doi: 10.1007/978-3-319-33310-6_3.

[28] C.R. Bauwens, S.B. Dorofeev, Effect of initial turbulence on vented explosion overpressures from lean hydrogen-air deflagrations, Int. J. Hydrogen Energ. 39 (2014) 20509–20515.

[29] H. Hisken, G.A. Enstad, V.D. Narasimhamurthy, Suppression of vortex shedding and its mitigation effect in gas explosions: an experimental study, J. Loss Prevent. Proc. 43 (2016) 242–254.

[30] M. Cross, G. Ciccarelli, DDT and detonation propagation limits in an obstacle filled tube, J. Loss Prevent. Proc. 36 (2015) 380–386.

[31] L.R. Boeck, M. Kellenberger, G. Rainsford, G. Ciccarelli, Simultaneous OH-PLIF and schlieren imaging of flame acceleration in an obstacle-laden channel, Proc. Combust. Inst. 36 (2017) 2807–2814.

[32] L.R. Boeck, S. Lapointe, J. Melguizo-Gavilanes, G. Ciccarelli, Flame propagation across an obstacle: OH-PLIF and 2-d simulations with detailed chemistry, Proc. Combust. Inst. 36 (2017) 2799–2806.

[33] V. Sakthitharan, Time-resolved measurements of flame propagation over baffle-type obstacles, PhD thesis, Imperial College London, 1995.

[34] R.P. Lindstedt, Deflagration to detonation transition in mixtures containing LNG/LPG constituents, PhD thesis, Imperial College London, 1984.

[35] R.P. Lindstedt, H.J. Michels, Deflagration to detonation transition in mixtures of alkane LNG/LPG constituents with O_2/N_2, Combust. Flame 72 (1988) 63–72.

[36] K.H.H. Goh, P. Geipel, R.P. Lindstedt, Lean premixed opposed jet flames in fractal grid generated multiscale turbulence, Combust. Flame 161 (2017) 2419–2434.

[37] O. Ronneberger, M. Raffel, J. Kompenhans, Advanced evaluation algorithms for standard and dual plane particle image velocimetry, The 9th International Symposium on Applied Laser Techniques to Fluid Mechanics, Lisbon, Portugal (1998).

[38] M. Raffel, J. Kompenhans, Error analysis for PIV recording utilizing image shifting, The 7th International Symposium on Applications of Laser Techniques to Fluid Mechanics, Lisbon, Portugal (1994).

[39] F. Hampp, R.P. Lindstedt, Quantification of combustion regime transitions in premixed turbulent DME flames, Combust. Flame 182 (2017) 248–268.

[40] B. Wieneke, Generic a-posteriori uncertainty quantification for PIV vector fields by correlation statistics, The 17th International Symposium on Applications of Laser Techniques to Fluid Mechanics, Lisbon, Portugal (2014).

[41] A. Melling, Tracer particles and seeding for particle image velocimetry, Meas. Sci. Technol. 8 (1997) 1406–1416.

[42] S.K. Sinha, Improving the accuracy and resolution of particle image or laser speckle velocimetry, Exp. Fluids 6 (1988) 67–68.

[43] K. Nishino, M. Samada, K. Kasuya, K. Torii, Turbulence statistics in the stagnation region of an axisymmetric impinging jet flow, Int. J. Heat Fluid Flow 17 (1996) 193–201.

[44] A. Stella, G. Guj, J. Kompenhans, M. Raffel, H. Richard, Application of particle image velocimetry to combusting flows: Design considerations and uncertainty assessment, Exp. Fluids 30 (2001) 167–180.

[45] A. Gomez, D.E. Rosner, Thermophoretic effects on particles in counterflow laminar diffusion flames, Combust. Sci. Technol. 89 (1993) 335–362.

[46] D. Bradley, C.M. Harper, The development of instabilities in laminar explosion flames, Combust. Flame 99 (1994) 562–572.

[47] D. Bradley, C.G.W. Sheppart, R. Woolley, D.A. Greenhalgh, R.D. Lockett, The development and structure of flame instabilities and cellularity at low Markstein numbers in explosions, Combust. Flame 122 (2000) 195–209.

[48] D. Bradley, T.M. Cresswell, J.S. Puttock, Flame acceleration due to flame-induced instabilities in large-scale explosions, Combust. Flame 124 (2001) 551–559.

[49] C.K. Law, G. Jomaas, J.K. Bechtold, Cellular instabilities of expanding hydrogen/propane spherical flames at elevated pressures: theory and experiment, Proc. Combust. Inst. 30 (2005) 159–167.

[50] V. Moccia, J.D. Alessio, Burning behaviour of high-pressure CH_4-H_2-air mixtures, Energies 6 (2013) 97–116.